Localized Approach to Galvanic Coupling in an Aluminum–Magnesium System

Loïc Lacroix,[a,*] Christine Blanc,[a,,z] Nadine Pébère,[a,**] Bernard Tribollet,[b,**] and Vincent Vivier[b,**]**

[a]*Centre Interuniversitaire de Recherche et d'Ingénierie des Matériaux, UPS/INPT/CNRS, ENSIACET, Université de Toulouse, 31077 Toulouse cedex 04, France*
[b]*Laboratoire Interfaces et Systèmes Electrochimiques, UPR 15 du CNRS, Université Pierre et Marie Curie, 75252 Paris cedex 05, France*

The corrosion behavior of a pure aluminum/pure magnesium couple in a weakly conductive sodium sulfate solution was investigated. Potential and current distributions on the surface of the model couple at the beginning of immersion were obtained by solving the Laplace equation using a finite element method algorithm. Magnesium acted as the anode of the system while oxygen and water were reduced on aluminum. Calculations predicted a large current peak at the Al/Mg interface related to a local increase in both Mg dissolution and oxygen and water reduction on aluminum, leading to a local pH increase. Optical and scanning electron microscope observations confirmed the strong dissolution of magnesium concomitantly with depassivation of aluminum at the Al/Mg interface. Local electrochemical impedance spectroscopy showed the detrimental effects of the galvanic coupling both on aluminum and magnesium.

There is significant interest in the corrosion behavior understanding of Cu-containing Al alloys, such as 2024 aluminum alloy (AA2024), which are of importance for aerospace applications due to their high strength-to-weight ratio. Consequently, the corrosion susceptibility of the 2XXX Al-alloy series has been studied for a long time.[1-7] The corrosion of AA2024 is caused by the heterogeneous microstructure of the alloy, developed to improve the mechanical properties of the material. Among the different coarse intermetallic particles present in AA2024, Al_2CuMg particles, also called S-phase particles, have been widely studied because, due to their reactivity, they constitute preferential initiation sites for corrosion.[8-13] Even though the influence of S phase on the corrosion resistance of aluminum alloys has been clearly shown, the mechanisms explaining the dissolution of the intermetallics, the copper enrichment, and the pit nucleation at these sites are still not clearly understood.[8-18] Authors usually refer to a galvanic coupling phenomenon between the particles and the surrounding matrix to explain experimental observations, i.e., Al and Mg dealloying combined with Cu enrichment of the particles. To study these phenomena, many authors have used local techniques[18-22] such as atomic force microscopy combined with scanning Kelvin probe force microscopy[20-22] which provides high lateral resolution when conventional electrochemical methods lack spatial resolution. Another alternative is to study the electrochemical behavior of model alloys that are representative of the different metallurgical phases but these alloys are often multiphase materials and their corrosion behavior remains intricate.[23-25] Recently, Jorcin et al.[26] showed that studying a simple system such as the pure Al/pure Cu couple was relevant to understand the corrosion mechanisms associated with copper-rich intermetallics in aluminum alloys. Indeed, the corrosion phenomena observed in the model couple are representative of the electrochemical reactivity of the copper-enriched S phase. Usually, S-phase particle dissolution can be described by a two-step mechanism consisting in Al and Mg dealloying, which leads to copper-enriched particles and then galvanic coupling between the surrounding matrix and the copper-enriched S-phase particles. The first step mainly involves Mg dissolution.[17]

Thus, in the present study, a pure aluminum/pure magnesium (Al/Mg) couple was considered, in which pure aluminum represents the matrix and pure magnesium the S phase of Al–Cu–Mg alloys, to model the first step of particle dissolution. After 10 h immersion in a 10^{-3} M Na_2SO_4 solution, ex situ observations of the samples were performed with an optical and a scanning electron microscope to reveal the corrosion morphology. In situ observations using an optical microscope were performed and completed by local electrochemical impedance mapping. In all cases, particular attention was paid to the Al/Mg interface. Calculations based on the resolution of the Laplace equation were carried out to describe the potential distribution along the electrode radius. On the basis of the experimental approach and the mathematical model, the interpretation of the corrosion phenomena occurring in the sample and particularly at the Al/Mg interface was proposed.

Experimental

Sample.— The sample consisted of a Al/Mg couple. Both materials were provided by Alfa Aesar. The center of a cylinder of pure aluminum (99.999 wt %) was bored out to a precise diameter. After heating to expand the bore, a cylinder of pure magnesium (99.9 wt %) of the same diameter was inserted. On cooling, the Al/Mg assembly presented a tight interface, avoiding any crevice corrosion due to surface defects. The cylinder diameters were chosen to obtain an aluminum/magnesium surface area ratio of about 10 (the radii were 1 and 0.32 cm for the aluminum and magnesium bars, respectively). The electrode was then embedded in an epoxy resin so that the exposed part of the electrode was disk shaped. Before immersion in the electrolyte, the disk electrode was mechanically polished with SiC papers up to 4000 grade and ultrasonically cleaned with ethanol, then with distilled water. The electrolyte was a 10^{-3} M Na_2SO_4 solution prepared with analytical grade chemicals in contact with air at room temperature.

Local electrochemical measurements.— The corrosion behavior of the model couple was studied by local electrochemical impedance spectroscopy (LEIS). The measurements were carried out with a Solartron 1275 system. The method used a five-electrode configuration.[27-29] The probe (i.e., a bielectrode allowing local current-density measurement) was stepped across a selected area of the sample. The analyzed part had an area of 24,000 $\times$ 24,000 μm and the step size was 500 μm in the X and Y directions. Admittance was plotted rather than impedance to improve the visualization of the mapping. The maps were obtained at a fixed frequency chosen in the present case at 1 Hz. The local impedance measurements were carried out in a low conductivity medium, i.e., 10^{-3} M Na_2SO_4 solution (10^{-4} S cm^{-1}), to optimize resolution. With the experimental setup used, only the normal component of the current could be measured.

Surface characterizations.— The samples were observed before immersion and after 10 h of immersion in 10^{-3} M Na_2SO_4 solution

* Electrochemical Society Student Member.
** Electrochemical Society Active Member.
z E-mail: christine.blanc@ensiacet.fr

by optical microscopy with an Olympus PMG3 microscope. In situ observations were also performed using this microscope. Finally, observations with a Leo 435VP scanning electron microscope were performed to obtain a better description of the corrosion morphology, particularly at the Al/Mg interface.

Theoretical Description of the Current and Potential Distributions in Solution

Numerical calculations were undertaken to provide a fine description of the potential and current distributions on the disk electrode surface and in the surrounding electrolyte. Simulations were performed using a finite element package Comsol Multiphysics with the conductive dc module in a two-dimensional (2D) axial symmetry. The mesh size was refined to obtain a numerical error lower than 0.05% evaluated from the net current of the system which is the sum of the current passing through the magnesium and aluminum electrodes. The boundary conditions for the numerical calculations were determined from the analysis of experimental measurements performed on individual Al and Mg electrodes.

Steady-state measurements.— Figure 1 shows the individual polarization curves plotted in a 10^{-3} M Na_2SO_4 solution for pure aluminum and pure magnesium, respectively. The corrosion potential of the model couple was obtained from an open-circuit potential measurement when the model couple electrode was immersed in the same electrolyte. The corrosion potential of the couple was stable after 1 h of immersion at about −1.85 V/SSE (SSE denotes saturated sulfate electrode). As can be seen in Fig. 1, such a value corresponds to an anodic potential for the Mg electrode and to a cathodic potential for the Al electrode. On the aluminum electrode, two cathodic reactions can take place simultaneously depending on the electrode potential. At less cathodic potentials, the oxygen reduction reaction dominates, whereas at more cathodic potentials water reduction becomes predominant. Kinetic parameters were obtained from the fitting of the experimental curve, assuming that both cathodic reactions follow Tafel kinetics and are reported in Table I. On the magnesium electrode, both dissolution of the metal and water reduction were taken into account because at the corrosion potential of the couple, the cathodic reaction is assumed to be non-negligible on Mg. From the literature, the corrosion behavior of pure Mg can be described by the following reactions[30]

$$Mg \rightarrow Mg^{+}_{ads} + e^{-} \quad [1]$$

and

$$Mg^{+}_{ads} \rightleftarrows Mg^{2+} + e^{-} \quad [2]$$

Moreover, Mg corrosion is controlled by the presence of a very thin oxide film (probably MgO). MgO acts as a protective film and Mg corrosion occurs in film-free areas.[30] To take into account the negative difference effect (NDE), a chemical reaction is also introduced

$$Mg^{+}_{ads} + H_2O \rightarrow Mg^{2+} + OH^{-} + \tfrac{1}{2}H_2 \quad [3]$$

From the anodic and cathodic plots (Fig. 1), kinetic parameters were also determined for Mg (Table I). However, for Mg, the determination of the kinetic parameters can be marred by mistakes because the NDE usually leads to an underestimation of the Tafel coefficient.[31]

Mathematical models and results of the simulation.— Figure 2 shows the potential distribution (the separation between each white line corresponds to a 5 mV potential drop) and the current distribution (lines perpendicular to the isopotential lines) on the disk electrode used in this study, calculated for an electrolyte conductivity of 3×10^{-4} S cm^{-1} (see below). When the electrode is immersed in the electrolyte, the potential Φ in the solution surrounding the electrode is governed by the Laplace equation

$$\nabla^2\Phi = 0 \quad [4]$$

The use of cylindrical coordinates (r,θ,z) allows Eq. 4 to be expressed as

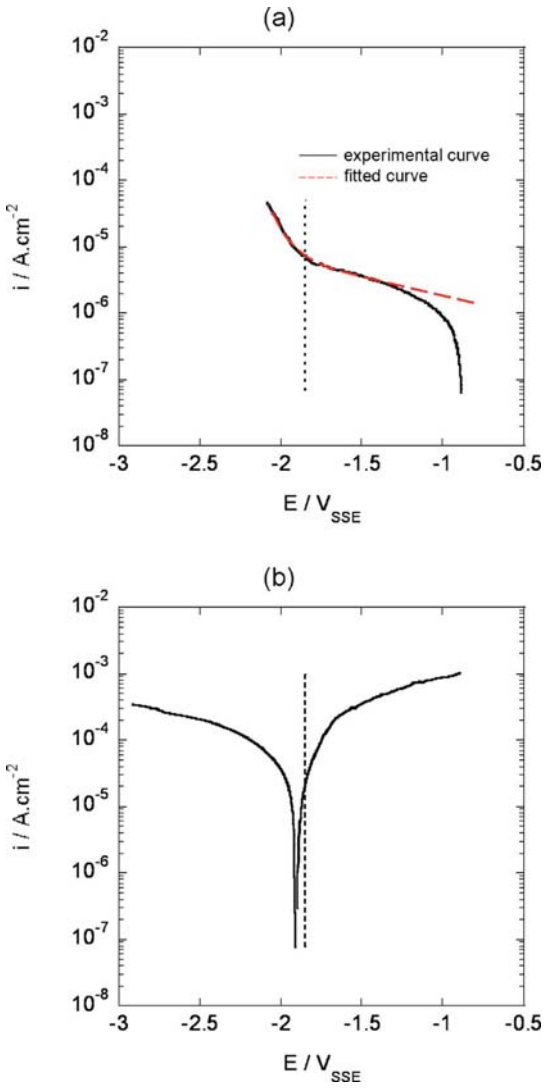

Figure 1. (Color online) (a) Cathodic polarization curve for pure aluminum (E_{corr} = −0.9 V_{SSE}) and (b) polarization curve for pure magnesium (E_{corr} = −1.9 V_{SSE}) in a 10^{-3} M Na_2SO_4 solution. Scan rate = 250 mV/h. The dotted line indicates the corrosion potential of the Al/Mg couple (E_{corr} = −1.85 V_{SSE}).

$$\frac{1}{r}\frac{\partial}{\partial r}\left(r\frac{\partial\Phi}{\partial r}\right) + \frac{1}{r^2}\frac{\partial^2\Phi}{\partial\theta^2} + \frac{\partial^2\Phi}{\partial z^2} = 0 \quad [5]$$

where z is the normal distance to the electrode surface, r is the radial coordinate, and θ is the azimuth. The cylindrical symmetry condi-

Table I. Kinetic parameters deduced from the polarization curves plotted for pure aluminum and pure magnesium in 10^{-3} M Na_2SO_4 solution.

Cathodic parameters (on Al)	$k^{Al}_{O_2}$ (A/cm^2) 5.60×10^{-6}	$b^{Al}_{O_2}$ (V^{-1}) 1.50	$k^{Al}_{H_2O}$ (A/cm^2) 1.97×10^{-6}	$b^{Al}_{H_2O}$ (V^{-1}) 13.81
Cathodic parameters (on Mg)	$k^{Mg}_{H_2O}$ (A/cm^2) 1.35×10^{-4}	$b^{Mg}_{H_2O}$ (V^{-1}) 1.1	—	—
Anodic parameters	k^{Mg}_{Mg} (A/cm^2) 6.8×10^{-3}	b^{Mg}_{Mg} (V^{-1}) 28.79	—	—

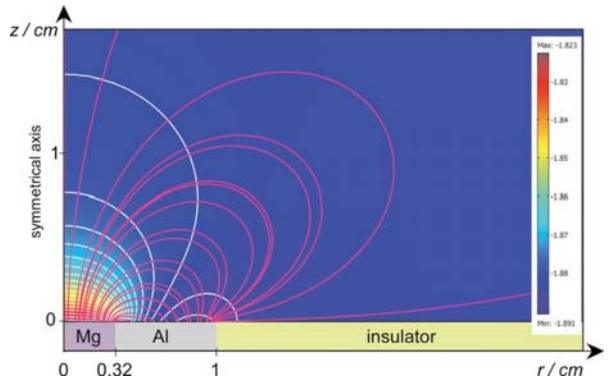

Figure 2. (Color online) Current and potential distributions in the solution ($\kappa = 3 \times 10^{-4}$ S cm^{-1}) due to the galvanic coupling of magnesium and aluminum.

tion requires the geometry to be invariant under rotation about the y axis, i.e.

$$\frac{\partial \Phi}{\partial \theta} = 0 \qquad [6]$$

The combination of Eq. 5 and 6 yields the governing equation in a 2D domain as

$$\frac{\partial^2 \Phi}{\partial r^2} + \frac{1}{r}\frac{\partial \Phi}{\partial r} + \frac{\partial^2 \Phi}{\partial z^2} = 0 \qquad [7]$$

On the surrounding insulator the boundary condition is given by

$$\left.\frac{\partial \Phi}{\partial z}\right|_{z=0} = 0 \quad \text{at } r > r_0 \qquad [8]$$

whereas far from the electrode surface, the potential tends toward zero, i.e.

$$\Phi \to 0 \quad \text{as } r^2 + z^2 \to \infty \qquad [9]$$

Under the assumption of a kinetic regime, the current density at the electrode surface can be expressed as

$$I = -\kappa \left.\frac{\partial \Phi}{\partial z}\right|_{z=0} \qquad [10]$$

where κ is the electrolyte conductivity.

As previously mentioned, on the aluminum electrode, two cathodic reactions can take place simultaneously and also the passive current (I_{pass}) must be considered. The value used in the calculations was $I_{pass} = 1$ μA cm^{-2}. The global current can be expressed as

$$I_{Al} = -k^{Al}_{O_2} \exp[b^{Al}_{O_2} \times (\Phi - V_{corr})] - k^{Al}_{H_2O} \exp[b^{Al}_{H_2O} \times (\Phi - V_{corr})] + I_{pass} \qquad [11]$$

On the magnesium electrode, the global current can be expressed as

$$I_{Mg} = k^{Mg}_{Mg} \exp[-b^{Mg}_{Mg} \times (\Phi - V_{corr})] - k^{Mg}_{H_2O} \exp[b^{Mg}_{H_2O} \times (\Phi - V_{corr})] \qquad [12]$$

where the constants k^{Mg}_{Mg}, b^{Mg}_{Mg}, $k^{Mg}_{H_2O}$, and $b^{Mg}_{H_2O}$ were determined from experimental measurements (Table I). Due to the corrosion potential of the model couple, active dissolution of magnesium occurs which can lead to a significant modification of the electrolyte conductivity. To take such variations into account, calculations were also performed for different values of κ.

Figure 3 shows the potential distributions calculated on the electrode surface and at 500 μm from the surface along the electrode radius with the electrolyte conductivity as a parameter. Independent of the electrolyte conductivity, the general shape of the potential

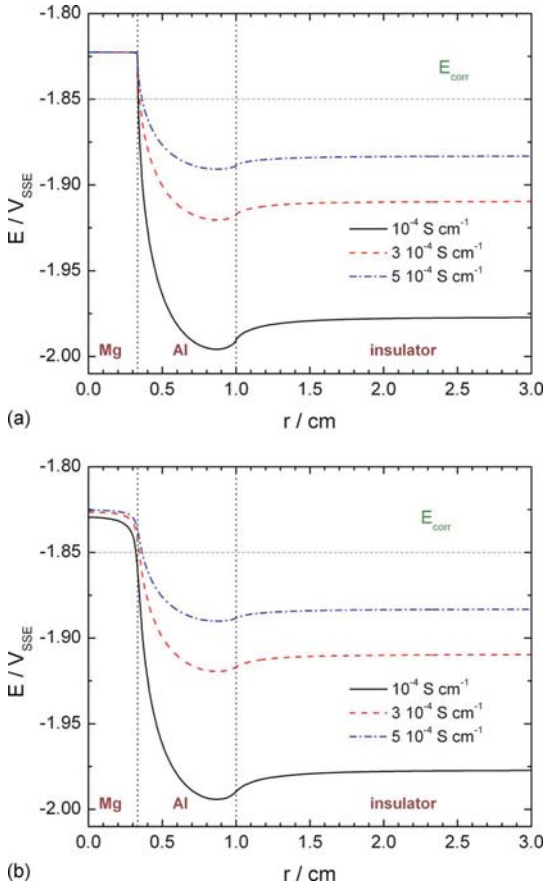

Figure 3. (Color online) Potential distributions calculated by finite element method (FEM) (a) at the electrode surface and (b) in solution 500 μm from the electrode surface with the electrolyte conductivity as a parameter.

distribution remains similar. The potential is constant over the magnesium electrode; it strongly decreases immediately after the Mg/Al interface and reaches a minimum value over the aluminum electrode near the Al/insulator interface just before a slight increase. Such behavior is fully consistent with the boundary conditions used for the calculation. Figure 3 also shows that the variations in the potential along the disk-electrode radius are greater for a low conductivity of the electrolyte which, from a practical point of view, made these variations easier to detect. Comparison of Fig. 3a and b shows the influence of the probe position. For a given conductivity, no significant difference was observed between the two calculated potential curves; however, when the probe was withdrawn from the electrode surface, the sudden variation in the potential at the Al/Mg interface was barely reduced by comparison to measurements performed on the disk-electrode surface itself.

The resolution of the Laplace equation also allows the distribution of the current on the disk-electrode surface to be determined: Both normal and radial current distributions were calculated (Fig. 4) with the solution conductivity as a parameter. Independent of the electrolyte conductivity, the general shape of the curves remains similar but the current values increase with conductivity. For the magnesium electrode, calculations show an anodic current varying along the electrode radius. The normal current distribution on magnesium shows that the current evolves toward infinite values at the Al/Mg interface, as observed by Verbrugge.[32] This is related to the discontinuity of the boundary conditions at the interface. The normal current on aluminum is almost constant but, for low conductivities, a slight increase in the cathodic current measured on aluminum can

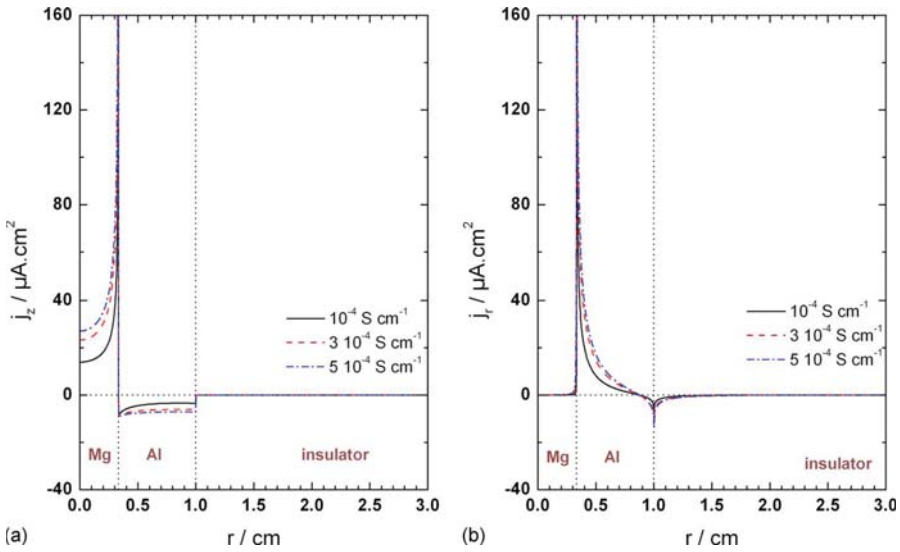

Figure 4. (Color online) Current distributions calculated by FEM at the electrode surface with the electrolyte conductivity as a parameter: (a) normal component and (b) radial component.

be seen at the Al/Mg interface. The distribution of the radial current is related to the potential distribution at the electrode surface. The constant potential on magnesium leads to a radial current equal to zero on this electrode while, for aluminum, the potential variation along the electrode radius leads to non-negligible current values with an increase in the radial component of the current in the vicinity of the Al/Mg interface. Both normal and radial current distributions were also calculated at a distance of 500 µm from the surface (Fig. 5). The general shape of the distributions remains comparable to the curves obtained at the electrode surface. For the normal component of the current, the values were almost identical except at the interface between the two metals: at the electrode surface, the normal current values evolved toward infinite values at the Al/Mg interface while they corresponded to finite values at a distance of 500 µm from the surface. The same difference between infinite and finite values was observed on the radial current distribution. Moreover, a non-negligible value of the radial current was measured on the Mg electrode particularly close to the Al/Mg interface because, for this distance, potential lines are no longer parallel to the electrode surface.

These analyses suggested a particular evolution of the interface morphology of the disk electrode after immersion in the electrolyte related to corrosion phenomena mainly localized at the Al/Mg interface.

Results and Discussion

Morphology of the Al/Mg interface.— Observations of the electrode surface were performed before, during, and after immersion. Figure 6 shows a scanning electron microscopy (SEM) micrograph of the Al/Mg couple before immersion. The two materials are joined without any defects observable at the interface. Figure 7 presents in situ optical microscopy observations of the Al/Mg couple during immersion in the 10^{-3} M Na_2SO_4 solution. As previously mentioned, in the Al/Mg couple, Al was the cathode and Mg was the anode. Observations showed that, from the beginning of immersion (4 min), the Mg electrode was corroded with hydrogen bubbles growing on the surface not only at the Al/Mg interface but also over its whole surface, in agreement with the dissolution mechanisms described before. The presence of hydrogen bubbles was attributed

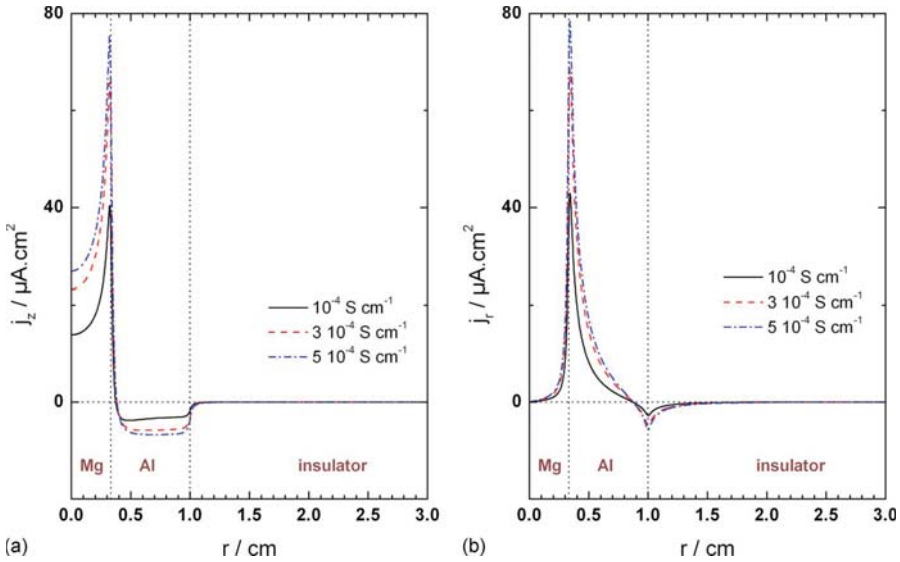

Figure 5. (Color online) Current distributions calculated by FEM in solution 500 µm from the interface with electrolyte conductivity as a parameter: (a) normal component and (b) radial component.

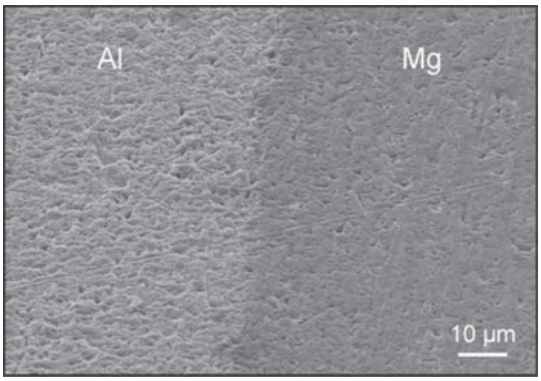

Figure 6. SEM observation of the Al/Mg interface before immersion.

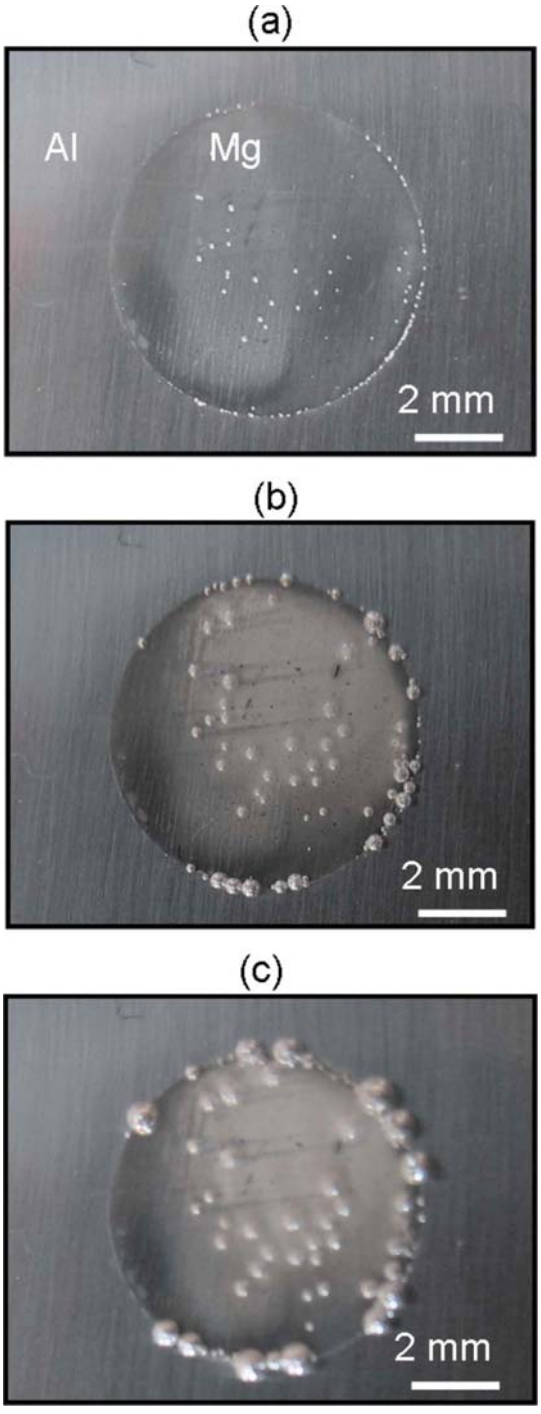

Figure 7. (Color online) In situ optical observations of the Al/Mg couple after immersion for (a) 4 min, (b) 20 min, and (c) 1 h in the 10^{-3} M Na_2SO_4 solution.

to the NDE (Reaction 3) which is favored by the increase in Mg dissolution due to the galvanic coupling. The hydrogen bubbles allowed active sites to be detected and comparison of Fig. 7a-c shows that the number and the locations of active sites did not change during immersion. Moreover, even though active sites were present over the Mg surface, observations showed that the Al/Mg interface was a preferential zone for Mg reactivity. Optical and SEM observations (Fig. 8) performed on the Al/Mg couple after 10 h of immersion in the 10^{-3} M Na_2SO_4 showed that abundant corrosion products, identified as $Mg(OH)_2$, occurred on the active sites shown in Fig. 7. The formation of $Mg(OH)_2$ (thick, porous corrosion product) is due to an increase in pH of the medium which induces the precipitation of insoluble species on the Mg surface, in agreement with the global corrosion process

$$Mg + 2H_2O \rightarrow Mg^{2+} + 2OH^- + H_2 \qquad [13]$$

When the corrosion products were removed, Mg corrosion was revealed mainly at the Al/Mg interface but also at a few locations on the Mg surface (Fig. 8b). Even if the presence of active zones corresponds to localized corrosion, it is not highly localized corrosion, such as pitting corrosion as occurs in aluminum and aluminum alloys. Here, the corrosion must be interpreted in terms of a more uniform type of corrosion as evidenced by the presence of the thick porous layer of corrosion products.[30] An accurate observation of the couple surface showed that pitlike features are seen on the Al surface (Fig. 8a and b). Figure 9 presents a SEM observation of the Al part after 10 h of immersion in the 10^{-3} M Na_2SO_4 solution, which shows the pitlike features. The corrosion of aluminum was observed only for long immersion times (some hours) far from the interface on the Al part of the model couple. Such a form of corrosion had also been observed on pure Al at high cathodic potentials. Figure 8c visualizes the Mg corrosion at the interface between the two materials; depassivation of aluminum near the interface was observed. This result was related to the high reactivity noted at the Al/Mg interface due to cathodic reactions (concomitant effect of both oxygen and water reduction) and anodic reaction (strong dissolution of magnesium) which contribute to a local alkalinization of the solution from the early stages of immersion particularly at the Al/Mg interface. Then, both anodic and cathodic reactions led to the increase in pH of the solution all over the surface of the Al/Mg couple. This led to the progressive depassivation of the aluminum surface which can explain the pitlike features. This type of localized corrosion does not correspond to the usual pitting corrosion observed in chloride-containing media but is mainly related to the pH increase which slowly dissolves the alumina film. To confirm this assumption, bromothymol blue was added to the Na_2SO_4 solution which had an initial pH of 5.7. This chemical turns blue when pH exceeds a value of 7.6. Figure 10 shows that the blue color appeared only a few minutes after immersion on the Mg electrode and near the Al/Mg interface on Al, indicating a rapid increase in the electrolyte pH. This shows that the kinetics of both cathodic reactions at the Al/Mg interface and Mg dissolution were strong enough to induce significant variations in pH in the electrolyte. After 1 h and 30 min of immersion, pH was higher than 7.6 all over the surface of the couple. Experimental results thus agree with theoretical calculations, showing a great reactivity of the Al/Mg interface.

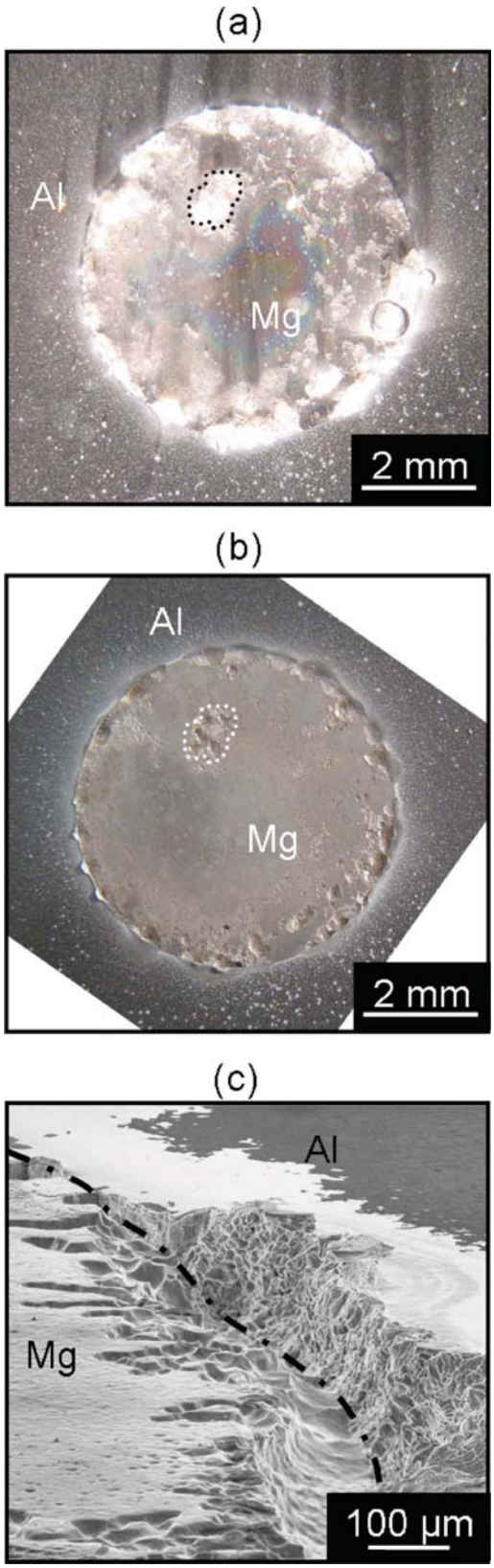

Figure 8. (Color online) (a) In situ, (b) ex situ optical, and (c) SEM observations of the Al/Mg couple after immersion for 10 h in the 10^{-3} M Na_2SO_4 solution.

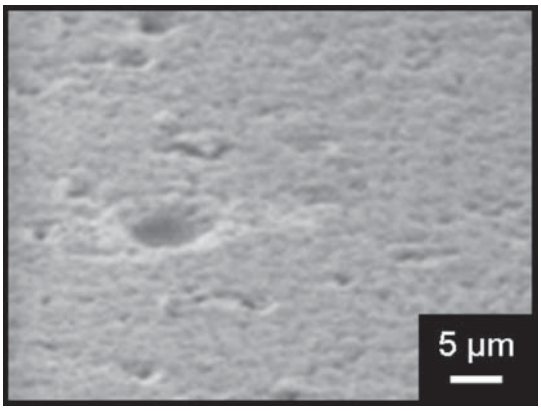

Figure 9. SEM observation of the Al part of the Al/Mg couple after immersion for 10 h in the 10^{-3} M Na_2SO_4 solution.

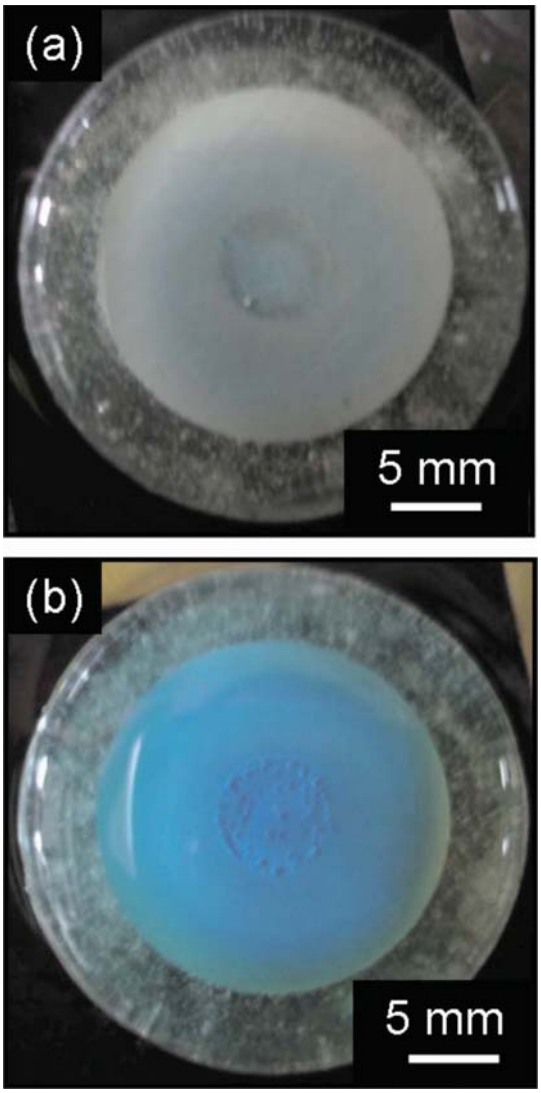

Figure 10. (Color online) In situ optical microscope observations of the Al/Mg couple after immersion for (a) a few minutes and (b) 1 h and 30 min in the 10^{-3} M Na_2SO_4 solution with bromothymol blue.

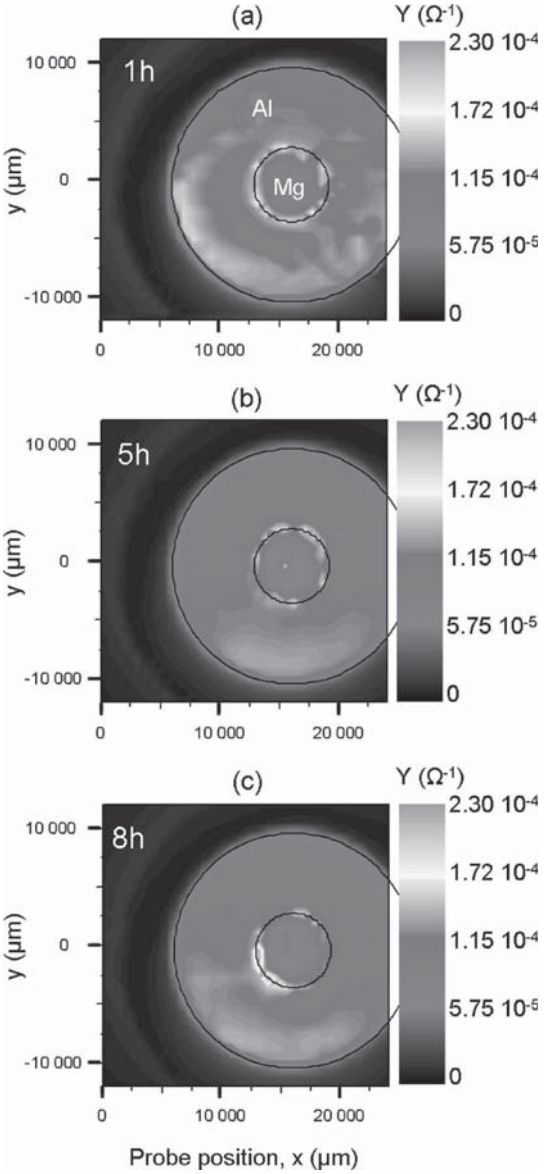

Figure 11. Local admittance maps of the Al/Mg electrode after (a) 1, (b) 5, and (c) 8 h of immersion in the 10^{-3} M Na_2SO_4 solution. $E = -1.85$ V/SSE. Frequency = 1 Hz.

LEIS measurements.— Figure 11 shows the local admittance maps plotted for the Al/Mg couple. The maps were obtained at the corrosion potential of the system (−1.85 V/SSE) after 1, 5, and 8 h of immersion in the 10^{-3} M Na_2SO_4 solution. The map plotted after 1 h of immersion showed high admittance values at the Al/Mg interface which corroborated both previous observations and the distribution of the current, indicating the high reactivity of the Al/Mg interface. Moreover, on the aluminum electrode, the admittance values were similar to those measured on magnesium which suggested the presence of a poorly protective passive film on aluminum. Comparison of Fig. 11a-c clearly showed the reactivity at the Al/Mg interface from early stages of immersion.

To sum up, the results showed that, in the Al/Mg couple, Mg was the anode while aluminum behaved as a cathode. Corrosion of magnesium was observed, leading to the alkalinization of the solution while oxygen and water were reduced on aluminum, also increasing the pH of the solution. Due to the galvanic coupling effect that can be observed in both the potential and current distributions, the reactivity was enhanced at the Al/Mg interface. This led to the alkalinization of the solution, particularly at the Al/Mg interface and then to the depassivation and the homogeneous dissolution of aluminum near the interface while Mg was found to be highly corroded. When the immersion time was increased, the solution pH also increased due to both anodic and cathodic reactions, which explains the progressive dissolution of the alumina film, leading to the presence of pitlike features.

Conclusions

The results show that model couples constitute an original and efficient approach to study corrosion mechanisms involving galvanic coupling. Here, the Al/Mg couple allowed the first step of the dissolution mechanism for Al_2CuMg particles to be analyzed. Combining the theoretical approach based on the resolution of the Laplace equation with experimental results obtained by using both microscopic observations and LEIS revealed a detrimental effect of the galvanic coupling both on aluminum and magnesium. The electrochemical response of the materials was largely influenced by the local pH. Such results are fully consistent with the electrochemical behavior of the S-phase particles for which strong Mg dissolution and depassivation of the surrounding Al matrix were observed.

Centre National de la Recherche Scientifique assisted in meeting the publication costs of this article.

References

1. J. W. J. Silva, A. G. Bustamante, E. N. Codaro, R. Z. Nakazato, and L. R. O. Hein, *Appl. Surf. Sci.*, **236**, 356 (2004).
2. A. Garner and D. Tromans, *Corrosion (Houston)*, **35**, 55 (1979).
3. X. Zhao, G. S. Frankel, B. Zoofan, and S. Rokhlin, *Corrosion (Houston)*, **59**, 1012 (2003).
4. X. Liu, G. S. Frankel, B. Zoofan, and S. Rokhlin, *Corros. Sci.*, **49**, 139 (2007).
5. J. F. Li, Z. Ziqiao, J. Na, and T. Chengyu, *Mater. Chem. Phys.*, **91**, 325 (2005).
6. V. Guillaumin and G. Mankowski, *Corros. Sci.*, **41**, 421 (1998).
7. W. Zhang and G. S. Frankel, *Electrochim. Acta*, **48**, 1193 (2003).
8. C. Blanc, B. Lavelle, and G. Mankowski, *Corros. Sci.*, **39**, 495 (1997).
9. C. Blanc, S. Gastaud, and G. Mankowski, *J. Electrochem. Soc.*, **150**, B396 (2003).
10. R. G. Buchheit, R. P. Grant, P. F. Hlava, B. McKenzie, and G. L. Zender, *J. Electrochem. Soc.*, **144**, 2621 (1997).
11. P. Campestrini, E. P. M. van Westing, H. W. van Rooijen, and J. H. W. de Wit, *Corros. Sci.*, **42**, 1853 (2000).
12. R. G. Buchheit, M. A. Martinez, and L. P. Montes, *J. Electrochem. Soc.*, **147**, 119 (2000).
13. R. G. Buchheit, L. P. Montes, M. A. Martinez, J. Michael, and P. F. Hlava, *J. Electrochem. Soc.*, **146**, 4424 (1999).
14. N. Birbilis and R. G. Buchheit, *J. Electrochem. Soc.*, **152**, B140 (2005).
15. C. Blanc, A. Freulon, M. C. Lafont, Y. Kihn, and G. Mankowski, *Corros. Sci.*, **48**, 3838 (2006).
16. Y. Yoon and R. G. Buchheit, *J. Electrochem. Soc.*, **153**, B151 (2006).
17. D. Zhu and W. J. van Ooij, *Corros. Sci.*, **45**, 2163 (2003).
18. T. Suter and R. C. Alkire, *J. Electrochem. Soc.*, **148**, B36 (2001).
19. M. Shao, Y. Fu, R. Hu, and C. Lin, *Mater. Sci. Eng., A*, **344**, 323 (2003).
20. P. Schmutz and G. S. Frankel, *J. Electrochem. Soc.*, **145**, 2285 (1998).
21. L. Lacroix, L. Ressier, C. Blanc, and G. Mankowski, *J. Electrochem. Soc.*, **155**, C8 (2008).
22. L. Lacroix, L. Ressier, C. Blanc, and G. Mankowski, *J. Electrochem. Soc.*, **155**, C131 (2008).
23. J. Idrac, C. Blanc, Y. Kihn, M. C. Lafont, G. Mankowski, P. Skeldon, and G. Thompson, *J. Electrochem. Soc.*, **154**, C286 (2007).
24. Y. Liu, E. A. Sultan, E. V. Koroleva, P. Skeldon, G. E. Thompson, X. Zhou, K. Shimizu, and H. Habazaki, *Corros. Sci.*, **45**, 789 (2007).
25. S. Garcia-Vergara, P. Skeldon, G. E. Thompson, P. Bailey, T. C. Q. Noakes, H. Habazaki, and K. Shimizu, *Appl. Surf. Sci.*, **205**, 121 (2003).
26. J. B. Jorcin, C. Blanc, N. Pébère, B. Tribollet, and V. Vivier, *J. Electrochem. Soc.*, **155**, C46 (2008).
27. G. Baril, C. Blanc, M. Keddam, and N. Pébère, *J. Electrochem. Soc.*, **150**, B488 (2003).
28. J. B. Jorcin, E. Aragon, C. Merlatti, and N. Pébère, *Corros. Sci.*, **48**, 1779 (2006).
29. J. B. Jorcin, M. E. Orazem, N. Pébère, and B. Tribollet, *Electrochim. Acta*, **51**, 1473 (2006).
30. G. Baril, G. Galicia, C. Deslouis, N. Pebere, B. Tribollet, and V. Vivier, *J. Electrochem. Soc.*, **154**, C108 (2007).
31. G. L. Song and A. Atrens, *Adv. Eng. Mater.*, **1**, 11 (1999).
32. M. Verbrugge, *Corros. Sci.*, **48**, 3489 (2006).